N-Doping of Graphene Through Electrothermal Reactions with Ammonia

Xinran Wang, *et al.*

Science **324**, 768 (2009);
DOI: 10.1126/science.1170335

Science (print ISSN 0036-8075; online ISSN 1095-9203) is published weekly, except the last week in December, by the American Association for the Advancement of Science, 1200 New York Avenue NW, Washington, DC 20005.

fact that the state that results from tracing over two modes in Eq. 1 still remains two-mode entangled (*28*). This property of $|W\rangle$ explains our observation of entanglement even in the face of complete dephasing between pairs *I* and *II* with 360° of phase noise.

We have also explored the transitions from fully separable to bipartite ($K = 1$), tripartite ($K = 2$), and quadripartite ($K = 3$) entangled *W* states by measuring the sum uncertainty as a function of two-photon suppression y_c, with our results presented in Fig. 4. With $\delta\phi = 0$, we obtained a uniformly low $\Delta \leq 0.08$ over a range in y_c from 0.035 to 1.37. These values of Δ are larger than in the two-mode case (Fig. 2B) and are explained by a small imbalance in $\hat{\rho}_W$ and by imperfections in the entanglement verification interferometers. Furthermore, these imperfections play an important role in the determination of the boundaries $\Delta_b^{(K)}$ for entanglement. As detailed in (*25*), small imbalances in the beamsplitter ratios of PBS$_{1,2}$ and BS$_{1,2}$ in Fig. 1C, and nonbalanced transmission losses lead to displacements of the boundaries toward smaller Δ, y_c. To reduce these boundary corrections, the beamsplitter ratios were all matched to 50%/50% to less than 3%, and the difference in losses of corresponding free-space and in-fiber optical paths were always held to less than 4%. Figure 4 shows the sizes of the corrections by displaying the boundaries $\Delta_b^{(K)}$ for the ideal lossless and balanced case as dashed lines.

In comparison to quantum-state tomography, our multipartite verification protocol features an exponential reduction in the number of measurements required to unambiguously detect entanglement. Specifically, our protocol requires us to determine 2^4 elements of $\hat{\rho}_W^{(r)}$ for y_c and 4 elements of $\hat{U}_{\text{ver}}^{\dagger}\hat{\rho}_W^{(r)}\hat{U}_{\text{ver}}$ for Δ, a total of 20 elements out of the $4^4 = 256$ that make up the reduced-density matrix $\hat{\rho}_W^{(r)}$. Our protocol inherently features the use of nonlocal measurements $\hat{M}_i$, thereby requiring only two experimental steps to measure all necessary elements and unambiguously detect entanglement in $\hat{\rho}_W$. Furthermore, the nonlinear structure of Δ allows the simultaneous detection of all possible realizations of Eq. 1 (*7*, *21*). These features alleviate the need for any complicated mechanism to control the measurement basis, which can be a challenge in tomography experiments (*16*) and other local measurement–based verification protocols for $\hat{\rho}_W$. Although linear witnesses might also enable entanglement detection with less than full knowledge of $\hat{\rho}_W$ obtained from a few experimental steps (*29*), the unambiguous verification of entanglement requires robustness in the face of experimental imperfections, including multiple excitations and losses (*25*).

Our study has introduced a new technique for the unambiguous verification of multipartite *W* states. Specifically, we examined entanglement in heralded quantum states specified by $\hat{\rho}_W$ with $N = 2,4$. Entanglement detected with our protocol refers to that of the complete density matrix $\hat{\rho}_W$ presented to our verification system, and not to fictitious components deduced via post selection (*6*). An extension of our protocol to different states (requiring increased experimental resources) is discussed in (*21*). Photonic entanglement, such as generated here, can be coherently mapped into atomic memories by way of electromagnetically induced transparency (*30*) for scalable quantum networks.

References and Notes

1. J. F. Clauser, A. Shimony, *Rep. Prog. Phys.* **41**, 1881 (1978).
2. A. Aspect, P. Grangier, G. Roger, *Phys. Rev. Lett.* **47**, 460 (1981).
3. M. A. Nielsen, I. L. Chuang, *Quantum Computation and Quantum Information* (Cambridge Univ. Press, Cambridge, 2000).
4. P. Zoller *et al.*, *Eur. Phys. J. D* **36**, 203 (2005).
5. H. J. Kimble, *Nature* **453**, 1023 (2008).
6. S. J. van Enk, N. Lütkenhaus, H. J. Kimble, *Phys. Rev. A* **75**, 052318 (2007).
7. O. Gühne, G. Toth, preprint available at http://arxiv.org/abs/0811.2803v2 (2008).
8. W. Dur, G. Vidal, J. I. Cirac, *Phys. Rev. A* **62**, 062314 (2000).
9. F. Verstraete, J. Dehaene, B. De Moor, H. Verschelde, *Phys. Rev. A* **65**, 052112 (2002).
10. R. Raussendorf, H. J. Briegel, *Phys. Rev. Lett.* **86**, 5188 (2001).
11. E. Knill, R. Laflamme, G. J. Milburn, *Nature* **409**, 46 (2001).
12. M. Hillery, V. Bužek, A. Berthiaume, *Phys. Rev. A* **59**, 1829 (1999).
13. S. Lloyd, *Science* **273**, 1073 (1996).
14. D. Leibfried *et al.*, *Nature* **438**, 639 (2005).
15. H. Haffner *et al.*, *Nature* **438**, 643 (2005).
16. W.-B. Gao *et al.*, preprint available at http://arxiv.org/abs/0809.4277v1 (2008).
17. L.-M. Duan, G. Giedke, J. I. Cirac, P. Zoller, *Phys. Rev. Lett.* **84**, 2722 (2000).
18. R. Simon, *Phys. Rev. Lett.* **84**, 2726 (2000).
19. S. L. Braunstein, P. van Loock, *Rev. Mod. Phys.* **77**, 513 (2005).
20. H. F. Hofmann, S. Takeuchi, *Phys. Rev. A* **68**, 032103 (2003).
21. P. Lougovski *et al.*, preprint available at http://arxiv.org/abs/0903.0851v1 (2009).
22. W. K. Wootters, *Phys. Rev. Lett.* **80**, 2245 (1998).
23. C. W. Chou *et al.*, *Nature* **438**, 828 (2005).
24. M. Reck, A. Zeilinger, H. J. Bernstein, P. Bertani, *Phys. Rev. Lett.* **73**, 58 (1994).
25. See the supporting material on *Science* Online.
26. L.-M. Duan, M. D. Lukin, J. I. Cirac, P. Zoller, *Nature* **414**, 413 (2001).
27. C.-W. Chou *et al.*, *Science* **316**, 1316 (2007).
28. C. F. Roos *et al.*, *Science* **304**, 1478 (2004).
29. H. Nha, *Phys. Rev. A* **77**, 062328 (2008).
30. K. S. Choi, H. Deng, J. Laurat, H. J. Kimble, *Nature* **452**, 67 (2008).

31. We gratefully acknowledge critical discussions with J. Laurat, P. Zoller, and J. Ye. This research is supported by IARPA, by NSF, and by NGST. S.P. and H.D. acknowledge support as Fellows of the Center for the Physics of Information at Caltech.

Supporting Online Material

www.sciencemag.org/cgi/content/full/324/5928/764/DC1
Methods
SOM Text
Figs. S1 to S5
Table S1
References

13 February 2009; accepted 18 March 2009
10.1126/science.1172260

N-Doping of Graphene Through Electrothermal Reactions with Ammonia

Xinran Wang,[1] Xiaolin Li,[1] Li Zhang,[1] Youngki Yoon,[2] Peter K. Weber,[3] Hailiang Wang,[1] Jing Guo,[2] Hongjie Dai[1]*

Graphene is readily p-doped by adsorbates, but for device applications, it would be useful to access the n-doped material. Individual graphene nanoribbons were covalently functionalized by nitrogen species through high-power electrical joule heating in ammonia gas, leading to n-type electronic doping consistent with theory. The formation of the carbon-nitrogen bond should occur mostly at the edges of graphene where chemical reactivity is high. X-ray photoelectron spectroscopy and nanometer-scale secondary ion mass spectroscopy confirm the carbon-nitrogen species in graphene thermally annealed in ammonia. We fabricated an n-type graphene field-effect transistor that operates at room temperature.

Recently, graphene has been made into semiconductors in the form of nanoribbons, leading to room temperature p-type graphene field-effect transistors (FETs) (*1*, *2*). However, a fundamental problem has been that the edge structures and chemical terminations of graphene synthesized by various methods are unknown and uncontrolled, whereas their effects to the physical properties have been widely predicted (*3*–*9*). In particular, graphene nanoribbons (GNRs) edge-terminated by nitrogen species were shown to be electron-rich, leading to n-type transistor behavior (*8*). Therefore, it is essential to precisely control the edge structures and chemical terminations to obtain desirable device characteristics. Edge doping could present a new means of doping for nanoscale graphene.

We now report that GNRs can be functionalized by nitrogen species by high-power electrical annealing (e-annealing) in NH$_3$ and exhibit n-type electronic doping. GNRs were synthesized chemically (*1*) or were lithographically patterned from pristine peel-off graphene (*10*–*12*); the

---

[1] Department of Chemistry and Laboratory for Advanced Materials, Stanford University, Stanford, CA 94305, USA. [2] Department of Electrical and Computer Engineering, University of Florida, Gainesville, FL 32611, USA. [3] Chemical Sciences Division, Lawrence Livermore National Laboratory (LLNL), Livermore, CA 94550, USA.

*To whom correspondence should be addressed. E-mail: hdai@stanford.edu

width ranged from below 10 nm up to ~150 nm. Chemically derived GNRs were dispersed on a 300-nm SiO_2/Si chip, located and imaged by scanning electron microscopy (SEM) with 1-kV acceleration voltage (*13*) and by atomic force microscopy (AFM) [Fig. 1, B and C, and fig. S1; see also supporting online material (SOM) (*14*)].

We then fabricated FET-like devices on selected ribbons with palladium (Pd) metal source/drain (S-D) and highly doped Si backgate (Fig. 1, A and D).

We first focused on GNRs wider than ~20 nm. Under ambient conditions, the edges of these as-made GNRs were probably terminated by hydrogen, oxygen, hydroxyl groups, and carboxylic groups (*15*) and exhibited p-doping with the Dirac point at gate voltage $V_{gs} > 40$ V in current-gate voltage I_{ds}-V_{gs} curves [fig. S3 (*14*)] (*1*, *2*). The p-doping was partly attributed to the oxygen edge groups (*6*, *7*), physisorbed oxygen molecules, and noncovalent poly(m-phenylenevinylene-co-2,5-dioctoxy-p-phenylenevinylene) (PmPV) coatings used in the synthesis process that are known to p-dope carbon nanotubes (*16*, *17*). Pumping in a vacuum reduced the conductance of GNRs slightly [fig. S3 (*14*)], corresponding to a decrease in p-doping by partial desorption of oxygen, either from the GNRs or GNR-metal contacts (*16*).

We then e-annealed the devices in high vacuum (~10^{-6} torr) by double sweeping the S-D bias V_{ds} (Fig. 2A). As V_{ds} was increased to high biases, the slope of I_{ds}-V_{ds} curve decreased or even became negative, with a noticeable hysteresis between back-and-forth sweeps that indicated the removal of the p-doping sources (*18*). We recorded I_{ds}-V_{gs} curves immediately after each e-annealing sweep and observed that the Dirac point gradually moved toward zero V_{gs} [fig. S2 (*14*)]. We continued to increase V_{ds} during I_{ds}-V_{ds} sweeps until no hysteresis occurred, which indicated that most of the *p*-doping was removed (Fig. 2A and fig. S2). After e-annealing, the I_{ds}-V_{gs} curve of GNR devices always showed the Dirac point at finite positive V_{gs} (typically 5 to 20 V) and slightly asymmetric hole and electron conduction (Fig. 2B). The residual p-doping was probably caused by oxygen species remaining on the edges (Fig. 3C) (*6*, *7*), as well as the doping

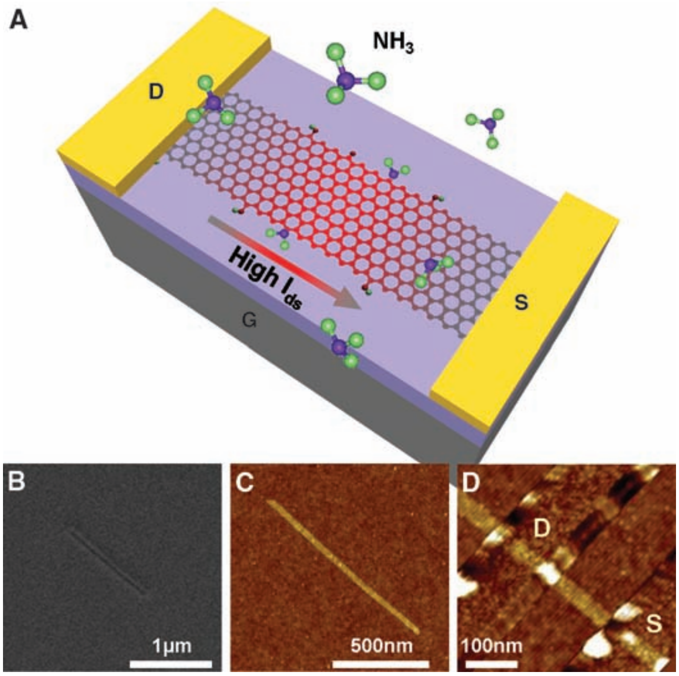

Fig. 1. Electrothermal reaction of individual GNRs in NH_3. (**A**) Schematics of a GNR device e-annealed under high current in NH_3. The devices have metal S-D, highly doped Si backgate and 300-nm SiO_2 gate dielectrics. The color gradient along the GNR represents the temperature profile: higher in the center region and lower near the contacts (*18*, *25*). Atomic colors are as follows: H, green; O, red; N, purple; C, gray. The GNR shown here is assumed to have ideal zigzag edges, which may not correspond to the GNRs in experiments. D, drain; S, source; G, gate. (**B**) SEM (acceleration voltage = 1 kV) and (**C**) AFM images of a ~30-nm-wide GNR. (**D**) AFM image of the device fabricated on the GNR shown in (B) and (C).

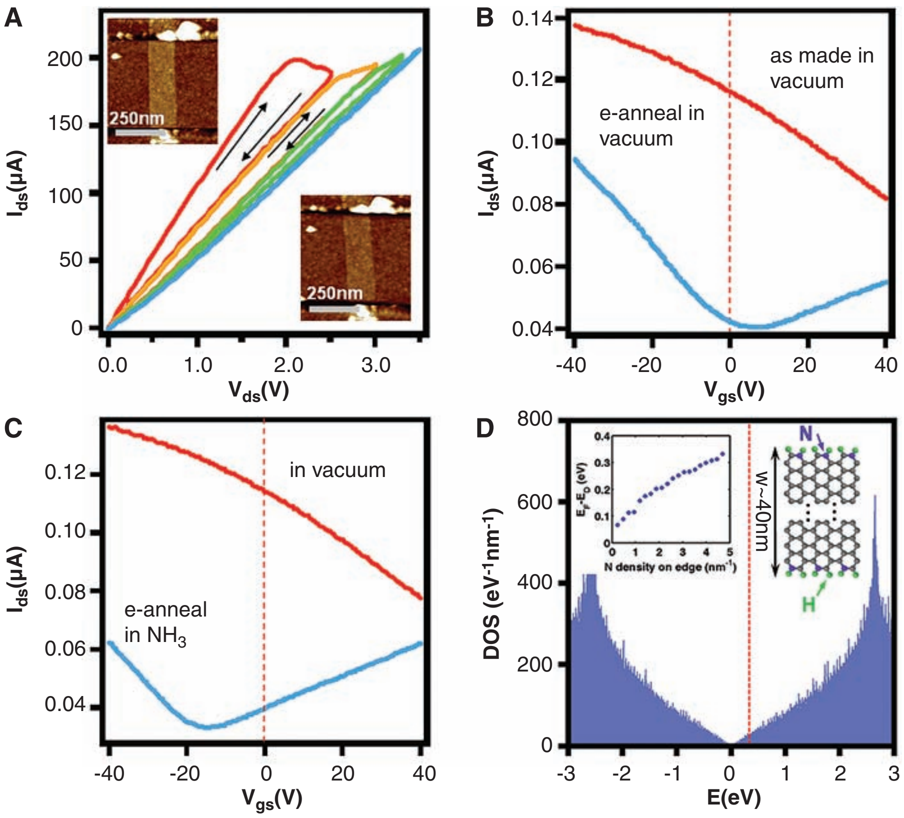

Fig. 2. E-annealing of individual GNRs in vacuum and NH_3. (**A**) Typical e-annealing process in vacuum for a *w* ~ 125-nm GNR. The process consisted of several double I_{ds}-V_{ds} sweeps (direction pointed by the arrows) with gradually increasing V_{ds}. We stopped when no hysteresis existed between back and forth sweeps (blue curve). (Upper and lower insets) AFM images of the same device as-made and after e-annealing in vacuum, respectively. The height was reduced from ~1.5 to ~1.0 nm because of removal of PmPV coatings by e-annealing. (**B**) I_{ds}-V_{gs} curves of the same GNR device as-made (red) and after e-annealing in vacuum (blue). The Dirac point moved from beyond 40 to ~8 V. (**C**) I_{ds}-V_{gs} curves of the same GNR device in vacuum before (red) and after e-annealing in NH_3 (blue). After e-annealing in NH_3, we pumped the device to base pressure for overnight before taking the blue curve. The Dirac point moved from beyond 40 to ~−14 V. V_{ds} = 1 mV in (B) and (C). (**D**) Calculated DOS of a *w* ~ 40-nm armchair GNR terminated partly by nitrogen species (*14*). The red dashed line denotes the Fermi level. (Left inset) The dependence of doping level (the position of the Fermi level from the Dirac point) on the density of substitutional N on the edges. (Right inset) Three unit cells of the simulated structure. There are two NH groups in the unit cell of the simulated structure. These edge groups are likely to coexist in real GNRs.

from the contact metal caused by the high work function of Pd (*19*).

During e-annealing, hundreds of microwatts of power were injected into a single GNR, which caused electrothermal self-heating of the GNR. We probed the temperature of GNRs under high-power input by measuring the red shift of the Raman G band of a single GNR (*14*, *20*). For a typical GNR under V_{ds} = 2 V (356-μW input power), a G-band shift of ~4.4 cm^{-1} was observed [fig. S5 (*14*)], corresponding to an average temperature of ~300°C along the GNR (*20*). Thus, electrical annealing of GNRs to hundreds of degrees led to the removal of physisorbed oxygen and PmPV molecules and reduced p-doping, consistent with the GNR height decrease by ~0.3 to 0.6 nm after e-annealing removal of the coating on GNRs (Fig. 2A, insets).

To chemically modify GNRs, we e-annealed the GNR devices in a ~1-torr NH_3/Ar environment with carefully designed sequences and control experiments [fig. S3 (*14*)]. In NH_3, we applied similar e-annealing sequences as in vacuum. After e-annealing, we pumped the chamber to base pressure for overnight (~8 hours) to fully remove physisorbed NH_3 molecules (*14*). Comparing the Dirac point positions of the devices in vacuum before and after e-annealing in NH_3, we observed a large ~–20-V shift (Fig. 2C and fig. S3B) that stayed stable and constant in vacuum. The shift caused by physisorbed NH_3 molecules (*21*) was usually smaller in magnitude [typically –5 V; fig. S3B (*14*)], and control experiments showed that physisorbed NH_3 molecules were unstable and removed in vacuum after overnight (~8 hours) pumping [fig. S3C (*14*)]. Considering the high temperature of GNRs during e-annealing in NH_3, we propose chemical reactions between GNRs and NH_3 leading to nitrogen functionalization, most likely at the more reactive edge carbon atoms (*15*). As a result, n-doping was introduced by the electron-rich nitrogen species (*8*). We cannot rule out the possibility of C–N bond formation at defect sites within the GNR plane; however, defect density in our chemically derived GNRs was low, based on their comparable electrical properties (including mobility, estimated to be a few hundred to ~1000 cm^2/Vs for GNRs wider than 20 nm) to similar-width lithographically patterned ribbons from pristine graphene (*2*). Furthermore, we carried out e-annealing of lithographically patterned GNRs from pristine peel-off graphene in NH_3 and qualitatively observed the same behavior as that of chemically derived GNRs [fig. S4 (*14*)]. These results suggest C–N formation most likely at the edge sites. Unlike the potassium doping approach (*22*), our doping approach introduced no appreciable charged impurities to degrade carrier mobility in GNR devices, as evidenced by similar p- and n-channel slopes in I_{ds}-V_{gs} curves before and after e-annealing in NH_3 (Fig. 2, B and C).

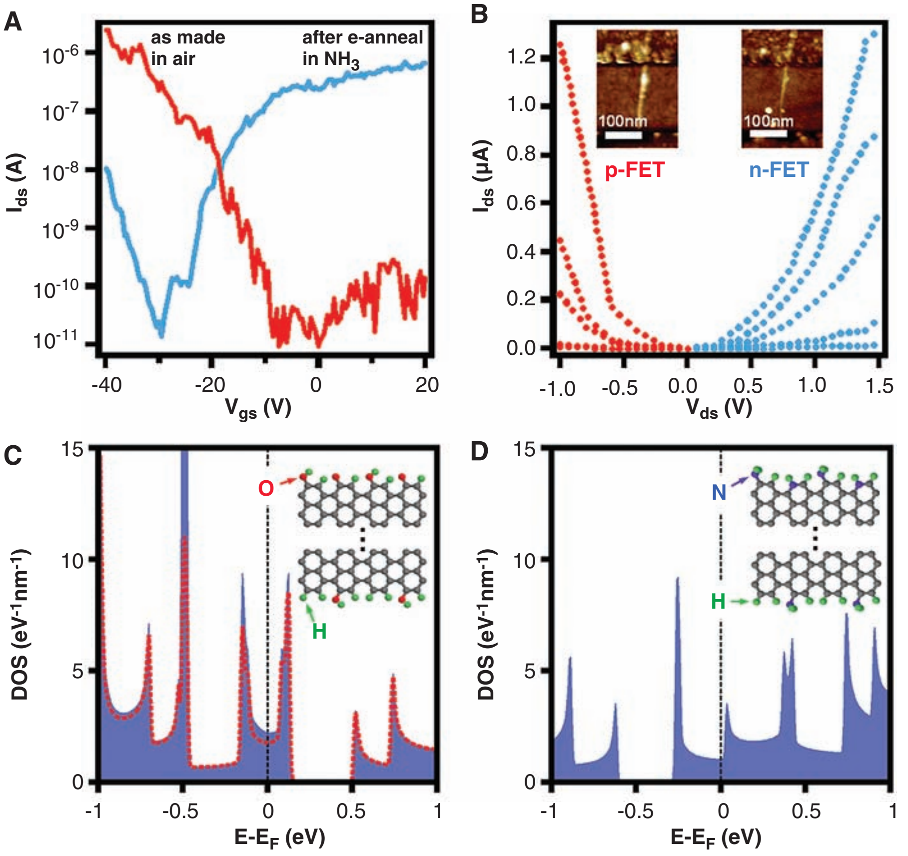

Fig. 3. Room temperature n-type graphene FETs. (**A**) I_{ds}-V_{gs} curves of the as-made GNRFET in vacuum (p-type, red) and after e-annealing in NH_3 (n-type, blue). V_{ds} = 1 V for both curves. (**B**) I_{ds}-V_{ds} curves of the same device. Red curves were taken on an as-made device: V_{gs} = –40 V, –37 V, –34 V, –31 V, and –28 V from top to bottom. Blue curves were taken on e-annealed device: V_{gs} = 40 V, 35 V, 30 V, 25 V, and 20 V from top to bottom. The nonlinear characteristics for both p- and n-type transistors near zero bias were due to finite SB for both electrons and holes by Ti contact used for this part of the work (*24*). Higher performance devices can be made by using higher (lower) work-function metals for p- (n-) type transistors and by heavily doping the contact regions, respectively. (Insets) AFM images of the device before and after e-annealing. Height was reduced by ~0.4 nm after e-annealing due to removal of PmPV coatings. (**C**) Calculated DOS of a semiconducting 21-armchair GNR (*w* ~ 2.5 nm) terminated by oxygen-containing groups (*14*). The red dashed line is the projected DOS (PDOS) on the carbon backbone, which clearly shows a p-type doping effect. (Inset) Two unit cells of the simulated GNR. There are one C=O and two C–OH groups in each unit cell. These edge groups are likely to coexist in real GNRs. E, energy; E_F, Fermi energy. (**D**) Calculated DOS of a 21-armchair GNR with nitrogen-containing groups on the edge sites, which is an n-type semiconductor (*14*). The DOS in the range of interest is mainly from the carbon atoms, and the PDOS on the carbon backbone has negligible difference with the total DOS within the energy range of interest. (Inset) Two unit cells of the edge structures of the simulated GNR. There are one NH and two C–NH_2 groups in each unit cell. These edge groups are likely to coexist in real GNRs.

We theoretically investigated the effect of edge functionalization by calculating the band structure of GNRs terminated by oxygen- and nitrogen-containing species (*14*). Calculations showed that GNRs with edge functionalization by oxygen and nitrogen species were p- and n-doped, respectively (Figs. 2D and 3, C and D), which agrees with the Dirac point shifts observed in experiments. P-doping was originated from a sub-band introduced near the Fermi level by edge C=O double bonds (Fig. 3C). A nitrogen atom bonded to two C atoms at the edges (that is, a N atom substituting a C atom at the edges, Figs. 2D and 3D) was the most effective in n-doping (*8*), whereas NH_2 groups terminating a GNR with perfect zigzag or armchair edges did not introduce n-doping (*7*). In real GNRs, however, the edges could be imperfect. N and NH substitution and NH_2 termination could all be possible after e-annealing, which leads to an n-doping effect (Fig. 3D). The n-doping level was approximately proportional to the density of edge substitutional N atoms in GNRs (Fig. 2D, inset). Under the same density of edge substitutional N atoms, the calculated doping concentration per unit area was found to scale inversely with the GNR width, which results in the Fermi level closer to the Dirac point for wider ribbons. Although the calculated structures were not the same as GNRs in our experiments, our calculations did confirm the possibility of "bulk" p- and n-doping of

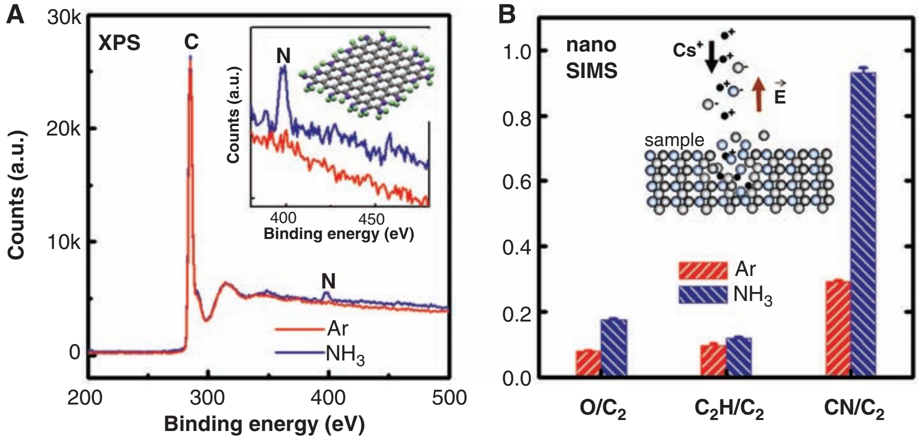

Fig. 4. Spectroscopy of GS films thermally annealed in NH_3 and Ar. (**A**) XPS on GS film thermally annealed in NH_3 (blue) and Ar (red, control sample). The peaks around 285 and 399 eV are assigned as C and N peaks, respectively. (Inset) Zoom-in view of the XPS data near the N peak. The sample annealed in NH_3 shows a clear N signal, whereas the control sample does not. (Sub-inset) Schematics of GSs thermally annealed in NH_3. a.u., arbitrary units. (**B**) Relative ionic O/C_2, CH_2/C_2, and CN/C_2 ratios detected by nanoSIMS (*14*). The sample annealed in NH_3 has a much higher CN/C_2 ratio than the control sample, indicating C–N bonds formed during thermal annealing in NH_3. The intensities and error bars are means and SEs from different regions of interest in the collection area. The finite N signal of control sample came from residual intercalant (tributyl ammonium hydroxide) used for making GSs (*23*). (Inset) Schematics of nanoSIMS experiment.

GNRs (up to width $w \sim 40$ nm) by edge chemical groups.

Direct spectroscopy of individual GNRs is difficult given the small quantity of the material and the limited spatial resolution of most spectroscopic tools, so we carried out x-ray photoelectron spectroscopy (XPS) and nanometer-scale secondary ion mass spectroscopy (nanoSIMS) studies on graphene sheet (GS) films (*23*) thermally annealed in NH_3 (*14*). Thermal reactions should give similar products as electrothermal reactions on graphene under similar reaction conditions. We thermally annealed a GS film under NH_3 to 1100°C and, as control, a similar film sample under Ar to 800°C. XPS data (Fig. 4A) revealed that both samples showed similar C signals, indicating a similar amount of carbon material measured. We observed a clear N signal on the sample annealed in NH_3, whereas we detected no N signal on the control sample (Fig. 4A, inset). From nanoSIMS (Fig. 4B), the sample annealed in NH_3 showed similar O/C_2 and C_2H/C_2 but greater CN/C_2 ratio than the control sample, suggesting C–N bond formation in GSs by thermal annealing. Both XPS and nanoSIMS data provided spectroscopic evidence of N atoms incorporated into graphene during thermal annealing in NH_3. Similar reactions were expected during electrothermal annealing of graphene. C–N bond formation should occur predominantly on the edges and defect sites in the plane, where the C atoms are much more chemically reactive than in the plane of perfect graphene (*15*). The observation of similar carrier mobilities after N-doping in our GNRs suggested no substantial bulk modification. However, the precise degree of bulk N substitution in graphene undergone reactions with NH_3 at various temperatures should be investigated systematically.

Tuning the electronic properties of graphene by chemistry of the edges and/or defects will have a large impact on graphene properties and applications. Previously, we demonstrated p-type sub–10-nm GNRFETs with as-made GNRs (*1*, *2*). In this experiment, we used the e-annealing approach in NH_3 to demonstrate n-type sub–10-nm GNRFETs operating at room temperature (Fig. 3). We used lower work-function metal Ti as the contact metal with a 5-nm Pd buffer layer to enhance electron conduction in the devices. As-made $W < \sim 5$ nm GNRFETs were p-type with I_{on}/I_{off} ratio ~ 10^5 (Fig. 3A), because of the aforementioned p-doping sources. We first e-annealed the GNRFETs in vacuum, after which the devices became ambipolar [fig. S6 (*14*)]. We then exposed the devices in NH_3, followed by e-annealing in NH_3. After e-annealing in NH_3, the GNRFET turned largely to n-type, with $I_{on} \sim 1\ \mu A$, I_{on}/I_{off} ratio ~ 10^5, and similar subthreshold slope as the as-made p-type GNRFETs. Physisorption of NH_3 alone had only weak effect on transistor characteristics with small difference between I_{ds}-V_{gs} curves in vacuum and NH_3 [fig. S6 (*14*)]. We never succeeded in making n-GNRFETs by simple NH_3 physisorption. The nonlinearity near zero bias in I_{ds}-V_{ds} curves for both n- and p-type transistors was due to finite Schottky barriers (SB) for both electrons and holes at Ti contacts (*24*). Ti contacts were used to observe a clear p- to n-FET evolution through the electrothermal reaction. For optimal device performances, one should use the highest and lowest possible work-function metal contacts for p- and n-type transistors respectively. Heavy doping at the contacts could also be invoked to improve performance. Ultra thin high-κ dielectrics could greatly improve the switching characteristics of p- and n-GNRFETs.

We calculated the density of states (DOS) of a semiconducting 21-armchair GNR (~2.5 nm wide) terminated by oxygen- and nitrogen-containing groups and observed p- and n-doping, respectively (Fig. 3, C and D), again confirming the edge chemical effects to the bulk properties of GNRs in the narrow-width regime. Taken together, the ability to control graphene chemistry is an important step toward controlled graphene electronics. Our results suggest that edge doping represents a new approach to dope graphene ribbons and affect its bulk properties, an interesting feature not likely in edge-free seamless carbon nanotubes. This technique, combined with precise control of edge shape (i.e., zigzag or armchair), may lead to precise determination of GNR device characteristics in the future. The current work also opens new possibilities of doing further chemistry on graphene.

References and Notes

1. X. Li, X. Wang, L. Zhang, S. Lee, H. Dai, *Science* **319**, 1229 (2008); published online 23 January 2008 (10.1126/science.1150878).
2. X. Wang *et al.*, *Phys. Rev. Lett.* **100**, 206803 (2008).
3. K. Nakada *et al.*, *Phys. Rev. B* **54**, 17954 (1996).
4. Y.-W. Son, M. L. Cohen, S. G. Louie, *Phys. Rev. Lett.* **97**, 216803 (2006).
5. D. Gunlycke, D. A. Areshkin, C. T. White, *Appl. Phys. Lett.* **90**, 142104 (2007).
6. D. Gunlycke *et al.*, *Appl. Phys. Lett.* **91**, 112108 (2007).
7. F. Cervantes-Sodi *et al.*, *Phys. Rev. B* **77**, 165427 (2008).
8. Q. Yan *et al.*, *Nano Lett.* **7**, 1469 (2007).
9. P. Zhao *et al.*, *Nano Res.* **1**, 395 (2008).
10. K. S. Novoselov *et al.*, *Science* **306**, 666 (2004).
11. Y. Zhang, T. Chen, H. L. Stormer, P. Kim, *Nature* **438**, 201 (2005).
12. K. S. Novoselov *et al.*, *Nature* **438**, 197 (2005).
13. T. Brintlinger *et al.*, *Appl. Phys. Lett.* **81**, 2454 (2002).
14. Experimental details and supporting data are available as supporting material on *Science* Online.
15. X. Wang, S. M. Tabakman, H. Dai, *J. Am. Chem. Soc.* **130**, 8152 (2008).
16. P. Avouris, *Acc. Chem. Res.* **35**, 1026 (2002).
17. H. S. Woo *et al.*, *Appl. Phys. Lett.* **77**, 1393 (2000).
18. J. Moser, A. Barreiro, A. Bachtold, *Appl. Phys. Lett.* **91**, 163513 (2007).
19. A. Javey *et al.*, *Naure* **424**, 654 (2003).
20. I. Calizo *et al.*, *Nano Lett.* **7**, 2645 (2007).
21. F. Schedin *et al.*, *Nat. Mater.* **6**, 652 (2007).
22. J.-H. Chen *et al.*, *Nature Physics* **4**, 377 (2008).
23. X. Li *et al.*, *Nat. Nanotechnol.* **3**, 538 (2008).
24. R. Martel *et al.*, *Phys. Rev. Lett.* **87**, 256805 (2001).
25. E. Pop *et al.*, *J. Appl. Phys.* **101**, 093710 (2007).
26. This work was supported in part by the Microelectronics Advanced Research Corporation Materials, Structures, and Devices Focus Center; Intel; and Office of Naval Research (ONR). The work done at the University of Florida was supported in part by NSF and ONR. The work at LLNL was performed under the auspices of the U.S. Department of Energy, contract DE-AC52-07NA27344.

Supporting Online Material

www.sciencemag.org/cgi/content/full/324/5928/768/DC1
Materials and Methods
SOM Text
Figs. S1 to S6
References

29 December 2008; accepted 13 March 2009
10.1126/science.1170335